

# First-principles modeling of plasmons in aluminum under ambient and extreme conditions

Kushal Ramakrishna,<sup>1,2,3,\*</sup> Attila Cangi,<sup>3</sup> Tobias Dornheim,<sup>3</sup> and Jan Vorberger<sup>1</sup>

<sup>1</sup>*Helmholtz-Zentrum Dresden-Rossendorf (HZDR), D-01328 Dresden, Germany*

<sup>2</sup>*Technische Universität Dresden, D-01062 Dresden, Germany*

<sup>3</sup>*Center for Advanced Systems Understanding (CASUS), D-02826 Görlitz, Germany*

(Dated: September 28, 2020)

The numerical modeling of plasmon behavior is crucial for an accurate interpretation of inelastic scattering diagnostics in many experiments. We highlight the utility of linear-response time-dependent density functional theory (LR-TDDFT) as an appropriate first-principles framework for a consistent modeling of plasmon properties. We provide a comprehensive analysis of plasmons from ambient throughout warm dense conditions and assess typical properties such as the dynamical structure factor, the plasmon dispersion, and the plasmon width. We compare them with experimental measurements in aluminum accessible via x-ray Thomson scattering and with other dielectric models such as the Lindhard model, the Mermin approach based on parametrized collision frequencies, and the dielectric function obtained using static local field corrections of the uniform electron gas parametrized from path integral Monte Carlo simulations both at the ground state and at finite temperature. We conclude with the remark that the common practice of extracting and employing plasmon dispersion relations and widths is an insufficient procedure to capture the complicated physics contained in the dynamic structure factor in its full breadth.

## I. INTRODUCTION

A consistent framework for modeling the properties of plasmons [1] in matter in the range from ambient to warm dense conditions is of utmost importance for both enhancing our fundamental understanding of extreme states of matter and supporting the diagnostics of scattering experiments [2]. As we will show, the properties of plasmons seem well understood under ambient conditions until one realizes that the data on plasmon dispersions and widths are actually sparse and rarely consistent between different experiments and theories. Capturing plasmon dispersion and width in experiment and theory becomes even more challenging under warm dense conditions [3].

Warm dense matter (WDM) is highly energetic and exhibits characteristics of solids, liquids, gases, and plasmas simultaneously [3–6]. Understanding WDM is essential for enhancing our knowledge about astrophysical objects, such as the physics in Earth’s core [7], the formation processes of both planets in our solar system [8–14] and of exoplanets [15, 16], in brown dwarfs [17, 18], and stellar interiors [19]. From a technological point of view, warm dense conditions arise in the heating process of inertial confinement fusion capsules on their path towards ignition [20, 21] and in the walls of high-power magnetic fusion devices [22].

Since both thermal and quantum effects have to be taken into account [23], the quality of well-established methods of plasma physics or of condensed-matter physics might be insufficient. Hence, an understanding of plasmons under warm dense conditions relies on innovative theoretical

tools and a close cooperation with experiments.

Experimental measurements of plasmons are carried out using several techniques such as x-ray Thomson scattering (XRTS) [24], electron energy-loss spectroscopy (EELS) [25], and inelastic x-ray scattering (IXS) at synchrotrons [26]. High pressures is induced using diamond anvil cells or (laser generated) shocks. Among these, the combination of high power optical lasers to generate WDM states and x-ray free electron lasers to diagnose them via XRTS is particularly useful [27], especially for studying astrophysical phenomena in the laboratory. Such an experimental setup is capable of achieving pressures on the order of a few Mbars and temperatures up to a few eVs. These experiments are nowadays performed at large-scale experimental facilities, such as SLAC [28] and the European XFEL [29]. Matter at even higher pressures and temperatures is investigated with highly energetic lasers at the NIF [30].

The measured XRTS scattering signal [24, 31–35] is directly linked to the numerical modeling of plasmons via the dynamic structure factor (DSF) [36]. The DSF is used as an important diagnostics for WDM [36], because systems parameters like the density and temperature are inferred from it.

The DSF and, thus, plasmons have been modelled theoretically with a number of different techniques. The basic understanding of dispersion and damping of plasmons (in a gas of electrons) stems from the random phase approximation (RPA) [37, 38]. It was then realized that the influence of electron-ion correlations on the plasmon damping is essential. This led to the Mermin dielectric function featuring generalized dynamic collision frequencies of screened Born or T-matrix type [39, 40]. Furthermore, combining local field corrections (LFC) with intra-species correlations was enabled in terms of the inter-species physics of the Mermin approach [41]. As

---

\* k.ramakrishna@hzdr.de

the collision frequencies of Born or T-matrix type were found to be insufficient for WDM, it was suggested to use the Kubo-Greenwood approach [42, 43] and density functional molecular dynamics (DFT-MD) to obtain the collision frequency instead [44, 45].

The logical extension of these prior plasma physics approaches is to simulate the system directly from first principles. Dynamic properties are obtained using linear response time-dependent density functional theory (LR-TDDFT). Here, Kohn-Sham (KS) orbitals incorporating all electron-ion correlations are used instead of the free particle states as in the traditional plasma physics methods mentioned earlier. Then, similar to before, an approximation in terms of the RPA or a LFC of the response function can be established. The difficulty lies in finding reliable, accurate, temperature- and frequency-dependent LFCs and exchange-correlation (XC) kernels [6, 45–48]. An even more advanced method is real-time TDDFT which, however, at this stage seems computationally too expensive to serve as a workhorse for computing plasmon properties [49].

In this paper, we present extensive LR-TDDFT results of the DSF, the plasmon dispersion, and the plasmon width of aluminium under ambient and warm dense conditions. We use different kernels and the latest (temperature-dependent) LFC obtained from fermionic path integral Monte Carlo simulations (PIMC) [50]. We compare these new results to a variety of theoretical and experimental data. We find insufficient agreement of our results with published data and many inconsistencies in the reported results. This means that the currently used XC functionals and kernels are not accurate enough to resolve remaining discrepancies between different experimental results.

Throughout this paper we work in atomic units, where  $\hbar = m_e = e^2 = 1$ , such that energies are expressed in hartrees and length in Bohr radii.

## II. METHODS

The goal of solving the many-particle Hamiltonian in an approximate fashion can be achieved in terms of methods like the RPA, LFC, DFT, and TDDFT. Electronic transport properties such as the dynamic response function, the dielectric function, and the DSF are computed based on these methods. We first introduce the general formalism and our notation, then we describe the relevant methods in more detail.

### A. The coupled electron-ion problem

Within the scope of non-relativistic quantum mechanics, the physics of coupled electrons and ions is governed by the many-particle Hamiltonian

$$\hat{H} = \hat{H}^i + \hat{H}^e + \hat{W}^{ei}, \quad (1)$$

with  $\hat{H}^i = \hat{T}^i + \hat{W}^{ii}$  denoting the kinetic energy and interaction of the ions,  $\hat{H}^e = \hat{T}^e + \hat{W}^{ee}$  the kinetic energy and interaction of the electrons, and  $\hat{W}^{ei}$  the interaction between the electrons and ions.

Furthermore, working within the Born-Oppenheimer approximation [51] reduces the solution of the coupled electron-ion problem to solving a Schrödinger equation for the electrons

$$\begin{aligned} \hat{H}^{BO}(\mathbf{r}_1, \dots, \mathbf{r}_{N_e}; \mathbf{R}_1, \dots, \mathbf{R}_{N_i}) \Psi_j(\mathbf{r}_1, \dots, \mathbf{r}_{N_e}) \\ = E_j^{BO}(\mathbf{R}_1, \dots, \mathbf{R}_{N_i}) \Psi_j(\mathbf{r}_1, \dots, \mathbf{r}_{N_e}), \end{aligned} \quad (2)$$

which depends parametrically on the coordinates of the underlying ionic structure through the potential energy surface  $E_j^{BO}(\mathbf{R}_1, \dots, \mathbf{R}_{N_i})$ . Here, the Born-Oppenheimer Hamiltonian is given by  $\hat{H}^{BO} = \hat{T}^e + \hat{W}^{ee} + \hat{W}^{ei} + \hat{W}^{ii}$ , where the  $N_e$  electrons have coordinates  $\mathbf{r}_j$ , while the  $N_i$  ions have mass  $M_I$ , charge  $Z_I$ , and coordinates  $\mathbf{R}_I$ .

### B. Dielectric response of the Born-Oppenheimer Hamiltonian

The *linear* response  $n_{ind}(\mathbf{q}, \omega)$  of the electronic system defined by the Born-Oppenheimer Hamiltonian in Eq. (2) to an external, time-dependent perturbation  $\delta v$  is given in Fourier space by

$$n_{ind}(\mathbf{q}, \omega) = \chi(\mathbf{q}, \omega) \delta v(\mathbf{q}, \omega), \quad (3)$$

where the proportionality factor corresponds to the density-density response function  $\chi(\mathbf{q}, \omega)$ . The dielectric function  $\epsilon(\mathbf{q}, \omega)$  is expressed in terms of the density-density response function as

$$\frac{1}{\epsilon(\mathbf{q}, \omega)} = 1 + \frac{4\pi}{q^2} \chi(\mathbf{q}, \omega). \quad (4)$$

Furthermore, the fluctuation-dissipation theorem [52] connects the DSF to the density-density response function

$$S(\mathbf{q}, \omega) = -\frac{1}{\pi n_e (1 - e^{-\omega/(k_B T_e)})} \text{Im}[\chi(\mathbf{q}, \omega)], \quad (5)$$

and, hence, to the dielectric function [53]

$$S(\mathbf{q}, \omega) = -\frac{q^2}{4\pi^2 n_e (1 - e^{-\omega/(k_B T)})} \text{Im}[\epsilon^{-1}(\mathbf{q}, \omega)], \quad (6)$$

where  $n_e$  is the free electron density and  $T$  the temperature. Note that throughout the paper, the theoretical methods we use, assume equilibrated temperature for ions and electrons. Hence, we use the term *temperature* to refer to both electronic and ionic temperature. Using the detailed balance relation for the DSF  $S(-\mathbf{q}, -\omega) = S(\mathbf{q}, \omega) e^{-\beta \hbar \omega}$ , diagnostics of parameters in experiments such as the temperature, the equation of state, ionization potential, and the density are inferred [36]. Traditionally, the DSF for WDM and high energy density matter is modelled using plasma based theories and various approximations. Recently *first-principles*

methods based on TDDFT have been successful in modeling XRTS spectra [35, 45, 49, 54].

Plasmons appear in the DSF as sharp peaks near the plasma frequency. They can be mathematically characterized as zeros of the complex dielectric function, emerge in the parameter range for which collective effects play a role in the response of the system, and are the dominant mechanism for very small wavenumbers [37, 55, 56].

### C. Plasmon properties from dielectric models and time-dependent density functional theory

#### 1. Random-phase approximation

The RPA has been applied widely in condensed matter, plasma, and nuclear physics to describe plasmons. They can be characterized as a collective property of a system of weakly interacting electrons (jellium model) surrounded by a uniform positive charge background [1, 57, 58]. Considering a highly dense system of electrons, the RPA provides the first improvement to the Hartree-Fock approximation.

The form of the RPA retarded dielectric function based on free electron states as used here is discussed in Refs. [37, 59, 60]. The imaginary and the real parts of the dielectric function are given by

$$\Im[\varepsilon(q, \omega)] = \sum_{a, s_a^z} \frac{4\pi\hbar^2 e_a^2}{q^2} \int \frac{d^3p}{(2\pi\hbar)^3} \times \delta[\hbar\omega + E(p) - E(p+q)] (f_a(p) - f_a(p+q)), \quad (7)$$

and

$$\Re[\varepsilon(q, \omega)] = 1 - \sum_{a, s_a^z} \frac{16\pi^2 m e^2 \hbar^2}{q^2} \mathcal{P} \int_{-\infty}^{+\infty} \frac{d^3p}{(2\pi\hbar)^3} p f(p) \times \frac{1}{2q} \left[ \log \left( \frac{pa_b}{\hbar} - \frac{qa_b}{2\hbar} - \frac{m\omega a_b}{q} \right) + \log \left( \frac{pa_b}{\hbar} - \frac{qa_b}{2\hbar} + \frac{m\omega a_b}{q} \right) \right], \quad (8)$$

where  $s_a^z$  accounts for the spin of the system for species  $a$ . The plasmon dispersion relation within the RPA is given by [38, 56]

$$\omega^2(q) = \omega_{pl}^2 \left[ 1 + \frac{\langle p^2 \rangle}{2m_e} \frac{q^2}{\omega^2(q)} + \dots \right], \quad (9)$$

where  $\omega_{pl}$  is the plasma frequency. The plasmon dispersion is obtained by fitting a parameter  $\alpha$  to [61]

$$\omega(q) = \omega_{pl}(0) + \alpha \frac{\hbar q^2}{m}, \quad (10)$$

as obtained from EELS and IXS experiments [62].

#### 2. Extended Mermin dielectric function

The RPA is not sufficient to account for strong correlations or even bound states. Introducing a dynamic damping or relaxation term  $\nu(\omega)$ , while maintaining density conservation, leads to the Mermin approach (MA) [39, 40]

$$\epsilon^{MA}(q, \omega) = 1 + \frac{[1 + i\nu(\omega)/\omega] [\epsilon(q, \omega + i\nu(\omega)) - 1]}{1 + \left[ i \frac{\nu(\omega)}{\omega} \right] \frac{\epsilon(q, \omega + i\nu(\omega)) - 1}{\epsilon(q, \omega \rightarrow 0) - 1}}, \quad (11)$$

which takes into account electron-ion collisions. The dielectric function  $\epsilon(q, \omega + i\nu(\omega))$  may be taken from the RPA using the dynamic collision frequency. The latter is obtained in screened Born or T-matrix approximation [40], or is computed using the Kubo-Greenwood approach based on KS orbitals and eigenvalues [44, 45].

#### 3. Local field corrections

LFCs are defined such that the full response function can be obtained from a convolution of the free density response function  $\chi^0(q, \omega)$

$$\chi(q, \omega) = \frac{\chi^0(q, \omega)}{1 - V(q)[1 - G(q, \omega)]\chi^0(q, \omega)}. \quad (12)$$

Additionally, electron-electron correlations are accounted for by including a LFC,  $G(q, \omega)$ , as in Ref. [41]

$$\epsilon(q, \omega) = 1 - \frac{1 - \epsilon^{RPA}(q, \omega)}{1 + G(q, \omega)(1 - \epsilon^{RPA}(q, \omega))}, \quad (13)$$

which leads to a dielectric function via Eq. (11) of extended Mermin type.

While the electronic LFC of a realistic system like warm dense aluminium intrinsically depends on the ionic component as well, the full problem typically cannot be solved. Therefore, one often substitutes the correct  $G(q, \omega)$  of the full system by the LFC of a uniform electron gas at the same density and temperature.

Often quantum Monte Carlo (QMC) data for the LFC, and representations thereof, are restricted to the static limit  $\omega = 0$ . While such a static approximation would, in principle, constitute an uncontrolled approximation, it has recently been shown [63–65] that the frequency dependence of  $G(q, \omega)$  has a negligible impact for  $r_s \lesssim 4$ , which is the case for the conditions considered in this work.

The first accurate data for the static LFC  $G(q, 0)$  of the UEG have been obtained by Moroni *et al.* [67, 68] on the basis of ground-state QMC simulations. These data have subsequently been parametrized by Corradini *et al.* [69] (CDOP), and have been widely used to include electronic correlation effects in many-body theory. Unfortunately, their parametrization is limited to the zero temperature,

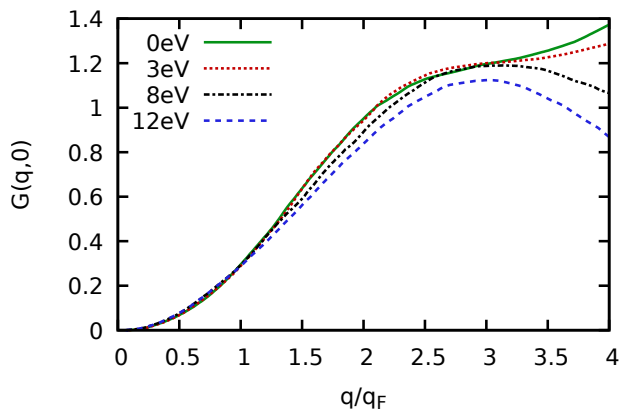


FIG. 1. Static LFC of aluminum ( $r_s = 2.07$ ) at four different temperatures. The data have been obtained from the machine-learning representation from Ref. [66].

which is often not sufficient for realistic WDM applications [70]. This problem has been overcome only recently by Dornheim *et al.* [66, 71–73], who presented a machine-learning representation of the static LFC (hereafter denoted as T-LFC) with respect to  $r_s$ ,  $\Theta = K_B T/E_F$ , and  $q$  on the PIMC data at finite temperature, covering the entire WDM regime, where  $E_F$  denotes the Fermi energy and  $K_B$  the Boltzmann constant.

The T-LFC is illustrated in Fig. 1 at the density of aluminum ( $r_s = 2.07$ ) for four different temperatures. For  $T = 0$  (solid green), the ML-representation reproduces the ground-state parametrization of CDOP. At  $T = 3$  eV (dashed red,  $\Theta \approx 0.26$ ), the effect of the temperature on  $G$  is small and only starts to manifest at large wavenumbers. Upon further increasing the temperature to  $T = 8$  eV (dash-dotted black,  $\Theta \approx 0.69$ ) significant deviations from the ground-state result are apparent, which are particularly pronounced for large  $q$  where the tail becomes negative. This is related to a lowering of the kinetic energy due to XC effects at these conditions, see Ref. [66] for an extensive discussion. Finally, the largest deviations are observed at  $T = 12$  eV (dashed blue,  $\Theta \approx 1.03$ ), where  $G$  is systematically lower than at  $T = 0$  for wavenumbers higher than the Fermi wavenumber. Therefore, we expect temperature effects of the LFC to be observable in our simulation results for temperatures  $T \gtrsim 8$  eV and wavenumbers  $q > q_F$ .

#### 4. Density functional theory coupled to molecular dynamics

In the framework of KS-DFT [74], a solution to Eq. (2) is found in a computationally feasible manner by introducing a fictitious system of non-interacting electrons that yields the same electronic density as obtained from directly solving Eq. (2). This is achieved by solving a set

of KS equations

$$\left[ -\frac{1}{2}\nabla_k^2 + V_s(\mathbf{r}) \right] \phi_k(\mathbf{r}) = \epsilon_k \phi_k(\mathbf{r}), \quad (14)$$

for the KS orbitals  $\phi_k$  from which the electronic density is constructed according to  $n(\mathbf{r}) = \sum_k^{N^e} \phi_k^*(\mathbf{r}) \phi_k(\mathbf{r})$ . Note that the solutions of the KS equations have a parametric dependence on the underlying ionic configuration  $\{\mathbf{R}_1, \dots, \mathbf{R}_{N_i}\}$  via the KS potential  $v_s(\mathbf{r}; \mathbf{R}_1, \dots, \mathbf{R}_{N_i}) = \sum_{I=1}^{N_i} Z_I/|\mathbf{r}_k - \mathbf{R}_I| + v_H[n](\mathbf{r}) + v_{XC}[n](\mathbf{r})$ , where  $v_H[n](\mathbf{r}) = \int d\mathbf{r}' n(\mathbf{r}')/|\mathbf{r} - \mathbf{r}'|$  denotes classical electrostatic interaction potential of a charge cloud (Hartree potential) and  $v_{XC}[n](\mathbf{r}) = \delta E_{XC}[n]/\delta n(\mathbf{r})$  the XC potential. While formally exact, in practice the XC energy  $E_{XC}[n]$  is unknown and approximations need to be used [75]. Furthermore, KS-DFT is generalized to finite temperature via Mermin’s theorem [76]. We follow the common approximation, where the explicit temperature dependence of the XC energy is neglected and only the implicit temperature dependence in the electronic density is taken into account. To that end, the temperature-dependent density is computed from the KS orbitals as  $n(\mathbf{r}) = \sum_k^\infty f_k(T) \phi_k^*(\mathbf{r}) \phi_k(\mathbf{r})$ , where  $f_k(T)$  denotes the Fermi-Dirac distribution at temperature  $T$ .

#### 5. Time-dependent density functional theory

LR-TDDFT [77] is a commonly used method to compute electronic response properties in a sufficiently accurate and computationally feasible manner. The formally exact, linear density response of the electronic system defined by the Born-Oppenheimer Hamiltonian given in Eq. (2) to an external, time-dependent perturbation  $\delta v(\mathbf{r}, t)$  is given as

$$\chi(\mathbf{q}, \omega) = \frac{\chi_s^0(\mathbf{q}, \omega)}{1 - [V(\mathbf{q}) - f_{XC}(\mathbf{q}, \omega)] \chi_s^0(\mathbf{q}, \omega)}, \quad (15)$$

where  $\chi_s^0$  denotes the KS density-density response function

$$\chi_s^0(\mathbf{r}, \mathbf{r}', \omega) = \lim_{\eta \rightarrow 0^+} \sum_{jk} (f_k(T) - f_j(T)) \times \frac{\phi_j(\mathbf{r}) \phi_j^*(\mathbf{r}') \phi_k(\mathbf{r}') \phi_k^*(\mathbf{r})}{\omega - (\epsilon_j - \epsilon_k) + i\eta}, \quad (16)$$

defined in terms of the KS orbitals and eigenvalues [46]. The electron-electron correlation is represented by the XC kernel which is formally defined as

$$f_{XC}(\mathbf{q}, \omega) = \chi_s^{-1}(\mathbf{q}, \omega) - \chi^{-1}(\mathbf{q}, \omega) - v(\mathbf{q}). \quad (17)$$

It is related to the XC potential via  $f_{XC}(\mathbf{q}, \omega) = \delta v_{XC}(\mathbf{q}, \omega)/\delta n(\mathbf{q}, \omega)$  and to the LFC of dielectric models via  $f_{XC}(\mathbf{q}, \omega) = -v(\mathbf{q})G(\mathbf{q}, \omega)$ , where  $v(\mathbf{q}) = 4\pi/q^2$ .

Virtually all practical calculations in LR-TDDFT employ a static (i.e., frequency-independent)  $f_{\text{xc}}$ , usually using the adiabatic local density approximation (ALDA). Further neglecting the XC kernel, i.e.,  $f_{\text{xc}} \rightarrow 0$ , yields what is called RPA calculations within the LR-TDDFT framework.

Then, plasmon properties such as the DSF are computed within the LR-TDDFT from the density-density response function through the fluctuation-dissipation theorem as before.

#### D. Computational Workflow

While we use the known perfect lattice structures for ambient conditions, we run DFT-MD simulations (usually using VASP [78–81]) for warm dense or high pressure conditions in order to generate snapshots of ionic configurations. A number of these unit or supercells of up to  $N = 32$  ions are then subject to a high resolution DFT calculation. Based on the resulting KS orbitals and various choices of LFCs and XC kernels, the density response function and, hence, plasmon properties are computed. Further details on all the technical parameters, settings, and certain convergence test results can be found in Appendix A.

### III. RESULTS

#### A. Ambient conditions

Solid aluminum has the space group  $\text{Fm}\bar{3}\text{m}$  in the cubic face centered (fcc) phase. Since the density of states of aluminium is close to the free electron result, we expect the plasmon dispersion to be described well by the RPA.

##### 1. Dynamic structure factor

The DSF at ambient conditions for a range of wavenumbers is shown in Fig. 2, where our calculations are compared to the nearest set of wavenumbers available from the literature [47, 82, 83].

We start our discussion with panel a) at a wavenumber  $1.08\text{\AA}^{-1}$  for which the system is clearly dominated by collective effects and the sharp plasmon carries most of the spectral weight. Correlations are important, as they shift the plasmon peak by roughly 2 eV compared to the free electron RPA result. These are mainly electron-ion correlations as can be deduced from the close resemblance of the TDDFT-XC, TDDFT-RPA, and TDDFT-LFC curves that all include different levels of electron correlations but the same KS orbitals (incorporating electron-ion correlations). Interestingly, similar calculations of Cazzaniga *et al.* [47] yielded an identical peak location, but a rather smaller peak height. This means that in

the energy range of the plasmon, Cazzaniga’s imaginary part of the response function is about a factor of 1.5 larger than in our calculations. Even more different is the shape and location of the experimentally determined plasmon peaks for this wavenumber. The two different experimental results are rather in agreement with each other [47, 82]. However, they are another factor of 1.5 smaller than Cazzaniga’s and therefore less than half as high as our results. Its location is lower by another eV. The differences appear even more pronounced if one takes into account that the considered wavenumbers are not identical.

We have to conclude that the KS orbitals (and therefore the XC functional used) are not sufficiently accurate to describe the influence of electron-ion correlation on the plasmons present in the structure factor of scattering experiments. This is surprising as other quantities calculated using DFT give rather good agreement, and aluminium is considered a simple metal.

Increasing the wavenumber of the perturbation as shown in panels b) to d) will lead to a broadening of the plasmon peak and finally to a mix of collective and single-particle effects which all contribute to the DSF.

Again, with increasing  $q$ , the TDDFT peaks remain shifted towards lower energies compared to RPA. The influence of LFC is best visible at large  $q$  when compared to the electron gas RPA giving a small reduction in the intensities at the peaks and a shift towards lower energies at small  $q$ . In the TDDFT results, the difference between no LFC and different types of LFCs (ALDA or CDOP) is less distinct, still the same trend of redshift remains. The effect of the LFC in aluminum has been determined experimentally by Larson *et al.* [84] for  $q$  up to  $4.37/\text{\AA}$ . They suggest a stronger impact at large wavenumbers predicted by calculations with LFCs.

The overall shape of the spectra continues to differ from the experimental results. While the maximum intensity is now in better agreement with the theoretical results, the TDDFT curves start to show a double peak structure still absent in the experimental curves displayed here. The overall peak position in our results remains shifted to higher energies as compared to the experimental and Cazzaniga’s theoretical results. The disagreement is even more worrying, when the higher number of bands,  $k$ -points and the number of explicitly treated electrons are taken into account in our calculations as compared to the earlier published results.

The two peak structure, displaying the plasmon and double plasmon excitations, is already accounted for by the non-interacting electron-hole bubble (and the band structure) and does not need higher order Coulomb correlations to appear. Inclusion of many-body effects, in the form of vertex correction, only improves the agreement with the experimental measurements at large  $q$  [85]. The inclusion of a nonlocal and dynamical XC kernel in TDDFT is further shown to improve the DSF in metals and semiconductors including the double-plasmon excitation [86–89]. Sturm *et al.* [90, 91] demonstrated that

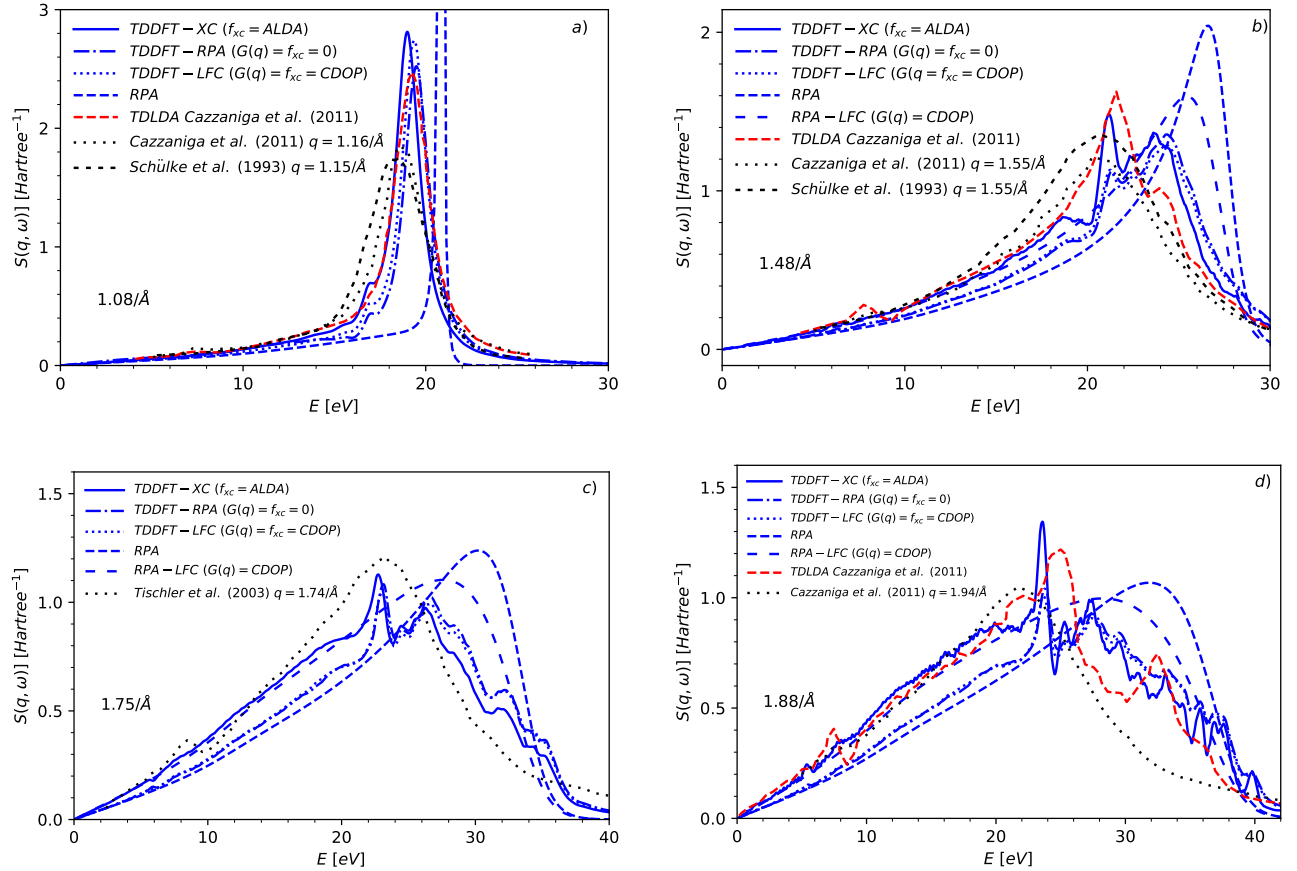


FIG. 2. DSF for aluminum in atomic units under ambient conditions at a) 1.08, b) 1.48, c) 1.75, and d) 1.88 ( $\text{\AA}^{-1}$ ).

Experimental data (in black) stems from Ref. 47, 82, and 83. Theoretical data (in red) stems from Ref. 47. TDDFT-RPA/TDDFT-XC/TDDFT-LFC/RPA/RPA-LFC results of this work are shown in blue. The scattering parameter  $\alpha = \kappa/q$ , with  $\kappa$  being the inverse screening length, is unity for  $q = 2.04/\text{\AA}$ , collective effects dominate for  $\alpha \ll 1$  [36, 56].

at large  $q$  and large frequencies dynamical correlation results in  $f_{xc}$  are more important than band structure effects in the description of the aluminum inelastic x-ray scattering. In summary, it seems that TDDFT overestimates the double plasmon excitations as in experiments they appear only at larger wavenumbers.

## 2. Plasmon dispersion

The plasmon dispersion under ambient conditions is shown in Fig. 3. The plasmon is stable up to the critical wavenumber ( $q_c$ ) with a quadratic dispersion feature and a flattening is observed for  $q > q_c$ .  $q_c$  is defined as the wavenumber at which the dispersion merges into the continuum of the single-particle excitations [98, 99]. For very small wavenumbers, in the optical limit, the Landau damping is very small [100] and the decay of the plasmon is mainly through electron-ion collisions [99]. Electron-electron interactions play an increasing role for increasing wavenumbers [56]. For wavenumbers above  $q_c$ , a plasmon cannot be defined based on many particle dielectric the-

ory [56], hence a shift based on the location of the peak of the DSF is given (Fig. 2). Intraband transitions are important to obtain the correct dispersion. Neglecting them would lead to a lower plasmon dispersion and deviation from the free electron gas model [97].

For small  $q$ , the various TDDFT approaches agree well with the theoretical results of Quong *et al.* [97] and the experimental measurements by Sprösser-Prou and Batson *et al.* [92, 93]. Near the critical wavenumber, we start to see deviations between experiment and different theoretical results, as already discussed in Fig. 2. This is due to the broadening of the plasmon peak and the onset of two-peak features in the DSF which complicates determining the peak position without determining the zeros of the dielectric function [56]. Therefore, we do not provide TDDFT results for the shift in the intermediate range.

For large  $q$ , the experimental results obtained by Batson [93] and H ohberger [94] *et al.* agree with our results. In this case, one should not speak of a plasmon anymore. The observed feature is better described by a shift of the peak of the DSF that is now dominated by single-particle

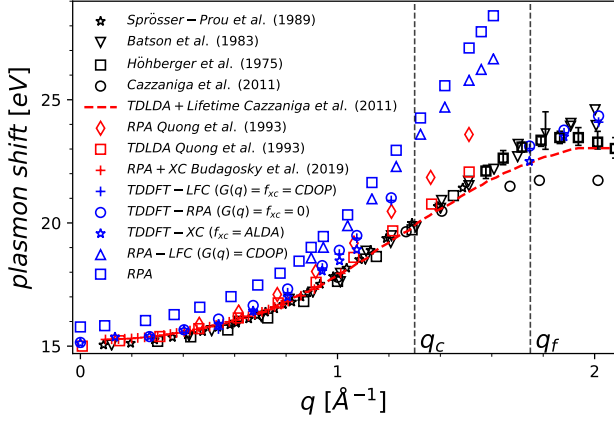


FIG. 3. Aluminum plasmon dispersion under ambient conditions. The critical and the Fermi wavenumbers are indicated by the vertical lines. Experimental data shown in black symbols stems from Ref. 47, 92–94. Theoretical data shown in red symbols are taken from Ref. 47, 95–97. TDDFT-RPA/TDDFT-XC/TDDFT-LFC/RPA-LFC/RPA results of this work are indicated with blue symbols.

excitations. The results of Batson [93] *et al.* show a flattening in the plasmon dispersion curve only for larger  $q$  as plotted.

The inclusion of different LFCs (TDDFT-LFC, CDOP Corradini *et al.* [69] and TDDFT-XC) results in a lowering of the plasmon shift at intermediate and large  $q$ . The influence of the TDDFT kernel compared to RPA in the lowering of the plasmon shift is also observed in the theoretical results of Quong and Cazzaniga *et al.* [47, 97]. Further improvements to the ALDA kernel can be achieved by considering an exact-exchange kernel (EXX) [101]. The inclusion of lifetime effects in TDDFT lowers the shift further as shown by Cazzaniga *et al.* [47]. However, the experimental results at large wavenumbers by Cazzaniga *et al.* [47] seem to contradict the results of Sprösser [92], Batson [93], and H ohberger [94]. This mainly illustrates the difficulty of extracting peak positions from structure factors at large  $q$ .

### 3. Plasmon width

The plasmon width under ambient conditions is shown in Fig. 4. The full width at half maximum (FWHM) is used to infer the width from the curves. This coincides with the plasmon damping as can be extracted from the Lorentz profile of the weakly damped plasmon at small wavenumbers. It can also be determined from finding the zeros of the complex dielectric function  $\epsilon[q, \omega(q) - i\gamma(q)]$  [56, 99].

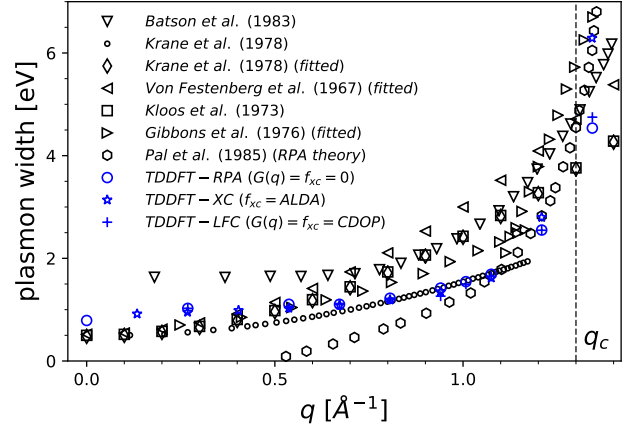


FIG. 4. Aluminum plasmon width under ambient conditions. The critical wavenumber is indicated by the vertical line. Experimental and theoretical data shown in black symbols stems from Ref. 62, 93, 102–105. TDDFT-RPA/TDDFT-XC/TDDFT-LFC results of this work are indicated with blue symbols.

The data is shown up to the wavenumbers near  $q_c$  where a stable plasmon feature is obtained from  $S(q, \omega)$ . The width calculated within TDDFT-RPA and TDDFT-XC has a flat feature for  $q < 1.0/\text{Å}$  and then grows rapidly with increasing  $q$  which can also be seen in the experimental measurements [62, 93, 102, 103]. The inclusion of LFC increases the width for  $q$  above  $q_c$  and has negligible impact for small  $q$  where the width is dominated by the electron-ion interactions which is taken into account in the DFT calculations. This is exemplified by the good agreement of TDDFT-RPA and TDDFT-XC for  $q < 1.0/\text{Å}$ . Significant deviations between the two emerge near  $q_c$  when the LFC has an increasing impact. However, the deviations between TDDFT-RPA and TDDFT-XC for the plasmon shift starts to appear at much smaller wavenumbers.

While the plasmon shift is in good agreement with the results of Batson *et al.* [93], the width given by Batson deviates from our results. Our results are in best agreement with the experimental results of Krane *et al.* [62] and, at small  $q$ , with the experimental results by Kloos *et al.* and Von Festenberg *et al.* [102, 103].

Furthermore, Krane *et al.* [62, 106] fit the experimental parameters  $\omega_{pl}(0)$  and  $\alpha'$  in Eq. (10) for  $q > 0.5/\text{Å}$  based on the change in the slope occurring at  $q \sim 0.5/\text{Å}$ . The plasmon linewidth determined from experiments [62] is

$$E_{1/2}^{pl}(q) = E_{1/2}^{pl}(0) + Bq^2 + Cq^4 + \dots, \quad (18)$$

where  $E_{1/2}^{pl}(0)$  is the plasmon linewidth in the optical limit,  $B$  (in  $\text{eV } \text{Å}^2$ ) [62, 102, 103] and  $C$  (in  $\text{eV } \text{Å}^4$ ) are the damping coefficients obtained experimentally.

Any experimental measurement, e.g., via XRTS, gives a  $q$ -dependent scattering signal featuring a plasmon shift and a width associated with it. Information on both

of these parameters are vital to benchmark (dynamic) LFCs, collision frequencies, and kernels in order to produce good TDDFT models. However, most experimental results available to us for ambient aluminum provide either the shift or the width with the exception of Batson *et al.* [93]. Thus, with the Batson data in its entirety not being consistent with our results and the lack of further consistent plasmon position and width data from experiment, the situation is very unsatisfactory. We are not even capable of comparing both plasmon position and width to other theoretical predictions due to lack of data.

## B. Extreme conditions

Measurements of the plasmon shift and width at extreme conditions of high pressure and temperature are quite challenging. Using isochoric heating by optical or x-ray pulses, solid aluminum foils are heated to high temperatures. Combining such a setup with x-ray and optical diagnostics, the electronic response of WDM [107] is accessed. Higher densities and, therefore, higher pressures can also be reached via isentropic or shock compression using high intensity laser pulses [34, 108]. The technical details of our TDDFT calculations are listed in Appendix A.

### 1. Plasmon dispersion

In Fig. 5, the plasmon shift is shown for densities  $2.7 \text{ g/cm}^3$  (uncompressed) and  $3.5 \text{ g/cm}^3$  (compressed) at a temperature of  $T = 0.3 \text{ eV}$ . Ideally, the temperature should have negligible impact on the plasmon shift, because it depends primarily on the electron density for degenerate matter. In general, the quadratic term in Eq. (9) is temperature dependent, but it is not for degenerate matter. The influence of any finite-temperature LFC (T-LFC),  $G(q, r_s, \Theta)$ , can be readily accessed based on the density, temperature and the momentum vector of the system (Table I in Appendix C). Due to extremely small  $\Theta = 0.02 - 0.025$ , temperature effects can be ignored in  $G(q, r_s, \Theta) \rightarrow G(q, r_s)$ . To this end, we also perform a comparison with RPA and TDDFT results computed at zero temperature ( $T = 0$ ).

When the static LFC is included, the plasmon shift decreases at large  $q$  and approaches the results obtained with TDDFT akin to the LFC approximation used for the XC kernel in TDDFT. Within the RPA, we also investigated the effect of treating the electrons within an all-electron basis versus a pseudopotential. We found that including the core electrons on a system size up to  $N = 32$  yields only an insignificant deviation on the shift from those calculated with the use of a pseudopotential. We compare our data for the uncompressed case at nominal  $T = 0.3 \text{ eV}$  with both the experimental measurements (black symbols) and the theoretical plasma physics models (green curves) of Witte *et al.* [44]. For small wavenum-

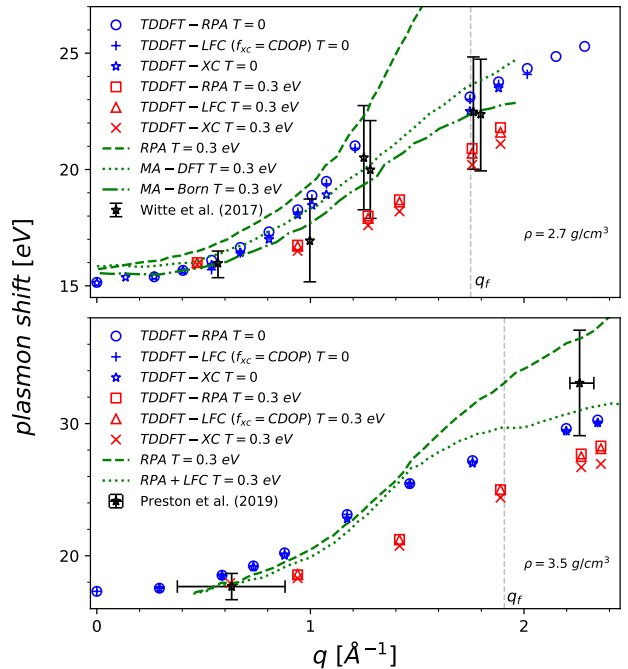


FIG. 5. Aluminum plasmon dispersion under extreme conditions ( $T=0.3 \text{ eV}$ ) for densities of  $2.7 \text{ g/cm}^3$  (uncompressed) and  $3.5 \text{ g/cm}^3$  (compressed). The Fermi wavenumber is indicated by the vertical line. Experimental and theoretical data for RPA, MA, RPA+LFC (in green) stems from Ref. 44 and 108. TDDFT-RPA, TDDFT-XC, and TDDFT-LFC results of this work are indicated with blue and red symbols.

bers, all our TDDFT results agree well with the experimental and other curves, which is mainly an indication that the density is correct. At larger wavenumbers, deviations are apparent which are caused by differing temperatures and different levels of approximations. Due to the large error bars, it is not possible to outright discard any theory with the exception of the pure RPA (green dashed). However, it seems that within the TDDFT results, there is no indication of the temperature being as extracted by Witte *et al.* [44]. The  $T = 0.3 \text{ eV}$  results (red) seem consistently lower compared to the measurements. A better agreement is reached when considering the ions at  $T = 0$  lattice positions and not in a molten state (blue symbols). This seems reasonable, as the time frame of the measurements is in the 100 fs range. In the compressed case, the available data set is restricted to two measurements, i.e., at small and large  $q$  [108]. At small  $q$ , the data agrees well with the experimental measurement which in this case is not trivial due to the shocked state of the system. Thus, the density determination seems reasonable. At large  $q$ , the TDDFT results are much lower than the experimental results due to the damping of the ions at the elevated temperature. Ignoring the temperature of the ions ( $T = 0$ ), the simulations are in better agreement with the experimental plasmon



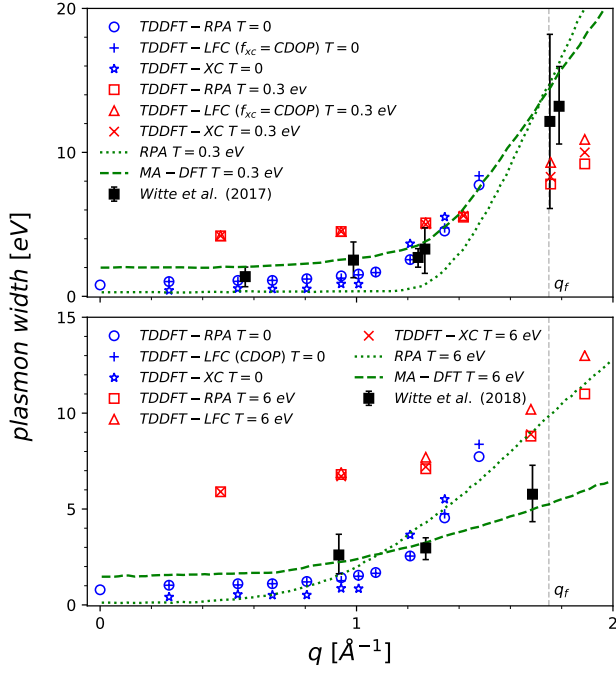


FIG. 6. Aluminum plasmon width under extreme conditions for  $\rho = 2.7 \text{ g/cm}^3$  at  $T = 0.3 \text{ eV}$  (above) and  $T = 6 \text{ eV}$  (below). The Fermi wavenumber is indicated by the vertical line. Experimental and theoretical data for RPA, MA (in green) stems from Ref. 44 and 109. TDDFT-RPA, TDDFT-XC, and TDDFT-LFC results of this work are indicated with blue and red symbols.

shift.

The transition from a quadratic dispersion to a flat feature can be observed at a smaller  $q$  when compared to aluminum at ambient density. RPA+LFC theory and TDDFT results indicate an increased damping with a raise in density (top versus lower panels in Fig. 5), but the experimental data remains inconclusive.

In summary, we find that the cold data ( $T = 0$ ) is in much better agreement with both XRTS measurements than the results obtained at  $T = 0.3 \text{ eV}$ . Of course, temperature measurements via XRTS, if not done via detailed balance, are always model dependent. We stress that LR-TDDFT using appropriate XC kernels or LFCs, respectively, is far more capable of including electron-electron as well as electron-ion correlations in the computation of collective effects and structure factors than any other theory.

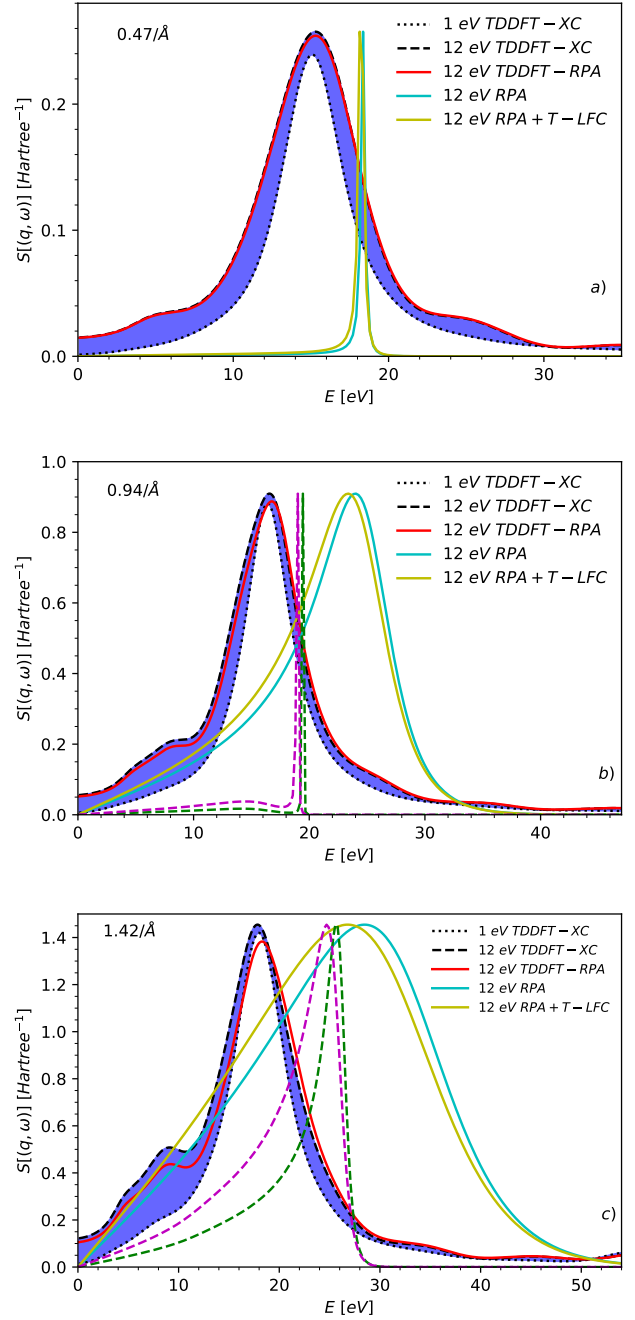


FIG. 7. DSF for aluminum in atomic units for a) 0.47, b) 0.94, and c) 1.42 ( $\text{\AA}^{-1}$ ) at various temperatures. The TDDFT-RPA results are shown only at 12 eV. The TDDFT-XC results are shown from 1 to 12 eV in the blue area (black curves for 1 and 12 eV) and are broadening with temperature. The purple and green dashed lines are the RPA and RPA+T-LFC results at 1 eV respectively. The RPA results are normalized with respect to the TDDFT-XC results at 12 eV to allow plotting them at the same scale.

## 2. Plasmon width

In Fig. 6, the plasmon width is shown for a density of  $2.7 \text{ g/cm}^3$  and temperatures of 0.3 and 6.0 eV. The data is compared to the available experimental results of Witte *et al.* and their calculations using plasma theory [44, 109]. Nominal at  $T = 0.3 \text{ eV}$ , the experimental data agrees well with the TDDFT results for the cold case. The width resulting from TDDFT in the cold case features a similar trend than the free electron gas where both methods agree for small  $q$ . At  $T = 0.3 \text{ eV}$ , the width is obtained from the linear response calculations involving DFT-MD snapshots. Here, the TDDFT results feature larger widths for small  $q$  but the data still lies within the large error bars of the experimental results at large  $q$ .

A similar trend can be observed for the case of  $T = 6 \text{ eV}$  as presented in the bottom panel of Fig. 6. The cold TDDFT results fit the experimentally determined width much better than the TDDFT data at elevated temperatures where the width is increased strongly due to the liquid structure of the ions.

Remarkably once again, the cold data is in much better agreement with the XRTS measurements than results at 0.3 eV and 6 eV data. Apart from the model-dependent temperature determination as mentioned above, this hints at the fact that the experimental time scales are too short to allow an equilibrium of the coupled electron-ion system to be established.

## 3. Temperature dependence of the DSF

In Fig. 7, the DSF of aluminum for various temperatures is shown. The usual dispersion and change in width of the plasmon can be observed in panels a) to c). For TDDFT, we notice that as long as the plasmon dominates the spectrum [panels a) and b)], the locations of the peaks at a specific  $q$  are independent of temperature. This is contrary to the prediction of the Lindhard-RPA (with and without LFCs, cyan and olive curves, respectively), for which the position of the plasmon changes drastically with temperature in panel b). Of course, temperature results in an increase of width in the plasmon peak. Once single-particle effects start to influence the structure factor for larger wavenumbers as in panel c), temperature causes a change in the position of the peak as predicted by TDDFT, too.

The inclusion of LFCs yields a downshift of the intensities to lower frequencies. Within TDDFT, also a slight increase of the peak height at large wavenumbers shown in panel c) is observed.

The influence of the finite-temperature LFC is only apparent at large  $q$  and at high temperatures, that is at 12 eV where a deviation from ground state LFC is observed in the energy range 0-10 eV. Table. I in Appendix C summarizes the LFCs considered in this work. We conclude that the temperature determination from

the plasmon peak and width is highly model dependent and great care should be taken in the choice of the applied theory.

## 4. Static structure factor

An important test of the quality of the DSF as presented in the preceding sections is given by the calculation of several different moments of the structure factor. Here, we focus on the calculation of the static structure factor from the TDDFT spectra according to

$$S(q) = \int_{-\infty}^{\infty} S(q, \omega) d\omega. \quad (19)$$

In Fig. 8, the electronic static structure factor of aluminum ( $r_s = 2.07$ ) within different theories is shown for several values of the degeneracy temperature  $\Theta$ . The red circles correspond to PIMC results for the uniform electron gas at  $\Theta = 0.75$  and are compared to RPA calculations including static LFCs both at finite temperature (T-LFC) and in the ground state (CDOP). The TDDFT-XC results are also shown for comparison in the temperature range up to 12 eV for  $q/q_F \lesssim 1.0$ . Note that only the contribution of the valence electrons is considered in the TDDFT-XC calculations. Furthermore, the TDDFT-XC results are limited to the displayed range of wavenumbers, because at higher values there are other excitations ( $L$ -edge, specifically with  $L_{2,3}$  and  $L_1$ ) that do not occur in an electron gas as considered in PIMC. Finally, the green curves have been obtained using the novel effective static approximation (ESA) [71], which has been shown to yield highly accurate results for  $S(q)$  over the entire WDM regime, with a typical systematic error of  $\sim 0.1\%$  as compared to PIMC.

The agreement between the integrated TDDFT spectra and the static structure from both PIMC and ESA is very satisfactory and serves as a benchmark of the quality of the TDDFT spectra.

## IV. CONCLUSIONS

We demonstrated the capabilities of LR-TDDFT in calculating plasmon location and plasmon width for the simple metal aluminium at ambient and extreme conditions. We studied aluminium as a perfect fcc lattice as well as an high pressure fluid. We used both all-electron codes and PAW pseudopotentials. Starting from TDDFT-RPA, we used a variety of XC kernels in the LR-TDDFT equations: ALDA, static  $T = 0$  LFCs, and temperature-dependent LFCs, the latter two based on QMC simulations.

We compared our results to plasma physics theories using the Mermin dielectric function and several different collision frequencies. Also, where available, we compared to experimental values.

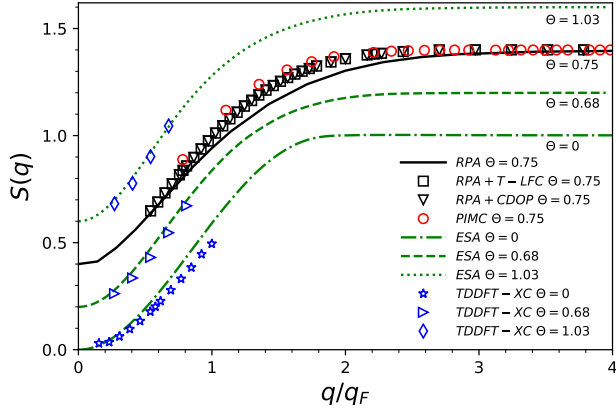


FIG. 8. Static structure factor for aluminum ( $r_s = 2.07$ ) computed using PIMC and RPA including LFCs at  $\Theta = 0.75$  ( $T = 8.77$  eV). The ESA results are shown for  $\Theta = 0$ ,  $\Theta = 0.68$  ( $T = 8$  eV) and  $\Theta = 1.03$  ( $T = 12$  eV). The TDDFT-XC results are shown from ambient to  $T = 12$  eV for  $q/q_F$  up to  $\sim 1.0$ .

Our analysis is based on relatively few complete data sets of both plasmon width and plasmon location (of which we present one) for aluminium at room temperature. Within this dataset, there is basically no consistent case in which two theories (or experiments) agree in plasmon location and width simultaneously. It is even more worrisome that TDDFT calculations that should be capable of obtaining very similar results (based on the published set of parameters and methods) fail to do so. While this is the case for aluminium at ambient conditions, the situation is naturally worse for warm dense, or high temperature aluminium where the error bars and uncertainties are larger due to experimental difficulties and computational challenges.

This has significant repercussions for the evaluation of experimental spectra from XRTS and other experiments, because such spectra are also used for temperature and density determination of the created states. While this is less problematic for states under ambient conditions or at high pressure in solids, it is a challenge for WDM states. XRTS is, in principle, one of the very few methods capable of obtaining such basic parameters which are used as input to subsequent simulation techniques. We, therefore, not only need accurate and reliable methods to calculate the dynamic structure but also fast methods to be able to fit spectra. Our assessment clearly points to a strong need for the development or improvements in reliable methods such as in LR-TDDFT.

#### ACKNOWLEDGMENTS

We are grateful to Maximilian Böhme for fruitful discussions and helpful comments. We thank Thomas Preston for the correspondence on experimental details regarding

compressed aluminum. We also thank Andrew Baczewski for the insightful input on TDDFT. We are also grateful to Chongjie Mo for providing the simulation data on aluminum. KR, TD and AC acknowledge funding by the Center for Advanced Systems Understanding (CASUS) which is financed by the German Federal Ministry of Education and Research (BMBF) and by the Saxon Ministry for Science, Culture and Tourism (SMWK) with tax funds on the basis of the budget approved by the Saxon State Parliament. Computations were performed on a Bull Cluster at the Center for Information Services and High Performance Computing (ZIH) at TU Dresden. We would like to thank the ZIH for its support and generous allocations of compute time.

## APPENDIX

### Appendix A: Computational details

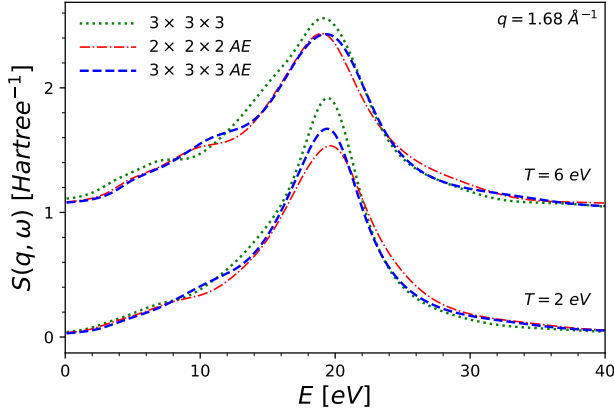


FIG. 9. DSF for aluminum ( $\rho = 2.7 \text{ g/cm}^3$ ) in atomic units at  $T = 2 \text{ eV}$  and  $T = 6 \text{ eV}$  with respect to  $k$ -points and the number of electrons considered in the pseudopotential. AE refers to the use of an all electron pseudopotential (11 electrons ignoring the  $1s^2$  core) compared to the 3 valence electrons otherwise.

At ambient conditions, the LR-TDDFT calculations were performed using the full-potential linearised augmented-plane wave code implemented in elk [110]. A  $k$ -point grid of  $40 \times 40 \times 40$  points was used and 80 bands were considered for the fcc unit cell. Fermi smearing was used with a width of 0.01 Ha. The adiabatic local density approximation (ALDA) as implemented in the elk code was used.

At WDM conditions, DFT-MD simulations were performed using VASP [78–81]. We used PAW pseudopotentials [111] with three electrons considered valence and a core radius of  $r_c = 1.7 \text{ a}_B$ . The plane wave cutoff was set to 350 eV and the convergence in each self-consistency cycle was set to  $10^{-5}$ . We used the Mermin formulation of thermal DFT [76] and Fermi occupation of the eigenvalues. Generally, the first Brillouin zone was sampled on a  $2 \times 2 \times 2$  grid of  $k$ -points. The number of bands varied with the temperature up to 1050 for the highest temperature of  $T = 12 \text{ eV}$  in a  $N = 32$  supercell. Both LDA [74] and PBE [112] XC functional were used. The thermostat in the NVT ensemble was of Nose-Hoover type [113]. Ionic time steps of  $\Delta t = 0.2 \text{ fs}$  were taken.

Simulations involving large system sizes at high temperatures and pressures are computationally too expensive within a full-potential linearised augmented-plane wave code. The KS orbitals for a supercell containing 32 aluminum atoms were, therefore, generated from DFT calculations on pseudopotential within Quantum ESPRESSO electronic structure code [114, 115]. The LDA norm-conserving pseudopotentials were generated with the OPIUM package [116]. 11 valence electrons were

considered in the pseudopotential, while the  $1s^2$  core is ignored. The plane-wave cutoff to represent the KS orbitals is set to 70 Ry. Electronic occupations are generated using a Methfessel-Paxton smearing [117] where the number of bands at a temperature of 12 eV is set to roughly 1050. The Brillouin zone was sampled using  $3 \times 3 \times 3$  Monkhorst-Pack mesh throughout. Based on these KS orbitals as input, LR-TDDFT were performed with the yambo [118], turboTDDFT [119] and TDDFPT [120, 121] packages.

The static limit of the LFCs is substituted in Eq. (12) as  $G(q, r_s)$  at ground state and as  $G(q, r_s, \Theta)$  at finite temperature.

### Appendix B: Convergence analysis of the DSF

The convergence with respect to the number of  $k$ -points and bands is important due to the computational cost. The DSF for aluminum at 2 eV and 6 eV using 32 atoms for 600 and 750 bands respectively is shown with respect to the  $k$ -points and the number of electrons considered in the pseudopotential in Fig. 9. The calculations are well converged with respect to the number of  $k$ -points. The all-electron (AE) LDA Perdew-Zunger norm-conserving pseudopotential results in a lowering of the peak intensity and an increase in the intensity to higher energies at the shoulder for  $T = 6 \text{ eV}$  at frequencies near 10 eV.

### Appendix C: Details on the local field corrections

The LFCs for aluminum at ambient and compressed densities ( $2.7$  and  $3.5 \text{ g/cm}^3$ ) in this work is shown in Table. I.

$\rho \text{ (g/cm}^3\text{)}$	$T \text{ (eV)}$	$q \text{ (\AA}^{-1}\text{)}$	LFC	T-LFC
2.7	1.0	3.02	0.79	0.79
2.7	3.0	3.02	0.79	0.79
2.7	6.0	3.02	0.79	0.76
2.7	8.0	1.89	0.33	0.34
2.7	8.0	2.36	0.53	0.51
2.7	8.0	2.83	0.72	0.67
2.7	8.0	3.02	0.79	0.74
2.7	12.0	0.47	0.02	0.02
2.7	12.0	0.94	0.08	0.09
2.7	12.0	1.42	0.19	0.20
2.7	12.0	1.89	0.33	0.34
2.7	12.0	2.36	0.53	0.48
2.7	12.0	2.83	0.72	0.63
3.5	0.3	1.89	0.29	0.29
3.5	0.3	2.36	0.45	0.45
3.5	0.3	2.83	0.63	0.63
3.5	0.3	3.02	0.70	0.70

TABLE I. Local field corrections (LFC) and finite-temperature LFCs (T-LFC) for aluminum at  $2.7$  and  $3.5 \text{ g/cm}^3$  for various temperatures and  $q$ -vectors.

- [1] David Bohm and David Pines, “A collective description of electron interactions. i. magnetic interactions,” *Phys. Rev.* **82**, 625–634 (1951).
- [2] National Research Council, *Frontiers in High Energy Density Physics: The X-Games of Contemporary Science* (The National Academies Press, Washington, DC, 2003).
- [3] F. Graziani, M. P. Desjarlais, R. Redmer, and S. B. Trickey, eds., *Frontiers and Challenges in Warm Dense Matter* (Springer, International Publishing, 2014).
- [4] V. E. Fortov, “Extreme states of matter on earth and in space,” *Phys.-Usp* **52**, 615–647 (2009).
- [5] T. Dornheim, S. Groth, and M. Bonitz, “The uniform electron gas at warm dense matter conditions,” *Phys. Reports* **744**, 1–86 (2018).
- [6] M. Bonitz, T. Dornheim, Zh. A. Moldabekov, S. Zhang, P. Hamann, H. Kählert, A. Filinov, K. Ramakrishna, and J. Vorberger, “Ab initio simulation of warm dense matter,” *Physics of Plasmas* **27**, 042710 (2020), <https://doi.org/10.1063/1.5143225>.
- [7] Dario Alfè and Michael J. Gillan, “First-principles calculation of transport coefficients,” *Phys. Rev. Lett.* **81**, 5161–5164 (1998).
- [8] B. Militzer, W. B. Hubbard, J. Vorberger, I. Tamblyn, and S. A. Bonev, “A massive core in jupiter predicted from first-principles simulations,” *The Astrophysical Journal* **688**, L45–L48 (2008).
- [9] J. Vorberger, I. Tamblyn, B. Militzer, and S. A. Bonev, “Hydrogen-helium mixtures in the interiors of giant planets,” *Phys. Rev. B* **75**, 024206 (2007).
- [10] M. Schöttler and R. Redmer, “Ab initio calculation of the miscibility diagram for hydrogen-helium mixtures,” *Phys. Rev. Lett.* **120**, 115703 (2018).
- [11] N. Nettelmann, A. Becker, B. Holst, and R. Redmer, *Astrophys. J.* **750**, 52 (2012).
- [12] N. Nettelmann, R. Helled, J. J. Fortney, and R. Redmer, *Planet. Space Sci.* **77**, 143 (2013).
- [13] W. Lorenzen, B. Holst, and R. Redmer, *Phys. Rev. Lett.* **102**, 115701 (2009).
- [14] W. Lorenzen, B. Holst, and R. Redmer, *Phys. Rev. B* **84**, 235109 (2011).
- [15] N. Nettelmann, J. J. Fortney, U. Kramm, and R. Redmer, “Thermal evolution and structure models of the transiting super-earth gj 1214b,” *Astrophys. J.* **733**, 2 (2011).
- [16] U. Kramm, N. Nettelmann, J. J. Fortney, R. Neuhauser, and R. Redmer, “Constraining the interior of extrasolar giant planets with the tidal love number  $k_2$  using the example of hat-p-13b,” *A & A* **538**, 8 (2012).
- [17] D. Saumon, W. B. Hubbard, G. Chabrier, and H. M. van Horn, “The role of the molecular-metallic transition of hydrogen in the evolution of jupiter, saturn, and brown dwarfs,” *Astrophys. J.* **391**, 827–831 (1992).
- [18] A. Becker, W. Lorenzen, J. J. Fortney, N. Nettelmann, M. Schöttler, and R. Redmer, “Ab initio equations of state for hydrogen (h-reos.3) and helium (he-reos.3) and their implications for the interior of brown dwarfs,” *Astrophys. J. Suppl. Ser* **215**, 21 (2014).
- [19] J. Daligault and S. Gupta, “Electron-ion scattering in dense multi-component plasmas: application to the outer crust of an accreting star,” *The Astrophysical Journal* **703**, 994–1011 (2009).
- [20] S. Atzeni and J. Meyer-ter Vehn, *The Physics of Inertial Fusion: Beam-Plasma Interaction, Hydrodynamics, Hot Dense Matter* (Clarendon Press, 2004).
- [21] S. X. Hu, B. Militzer, V. N. Goncharov, and S. Skupsky, “First-principles equation-of-state table of deuterium for inertial confinement fusion applications,” *Phys. Rev. B* **84**, 224109 (2011).
- [22] Toru Sasaki, Takuya Takahashi, Takumi Ohuchi, Yoshimasa Kawaguchi, Kazumasa Takahashi, Takashi Kikuchi, Tsukasa Aso, Nob. Harada, Kazuhiko Horioka, Hideo Nagatomo, and Shinsuke Fujioka, “Evaluation of transport properties in warm dense matter generated by pulsed-power discharge for nuclear fusion systems,” *Energy Procedia* **71**, 261 – 267 (2015), the Fourth International Symposium on Innovative Nuclear Energy Systems, INES-4.
- [23] M. D. Knudson and M. P. Desjarlais, “Shock compression of quartz to 1.6 TPa: Redefining a pressure standard,” *Phys. Rev. Lett.* **103**, 225501 (2009).
- [24] S. H. Glenzer, O. L. Landen, P. Neumayer, R. W. Lee, K. Widmann, S. W. Pollaine, R. J. Wallace, G. Gregori, A. Höll, T. Bornath, R. Thiele, V. Schwarz, W.-D. Kraeft, and R. Redmer, “Observations of plasmons in warm dense matter,” *Phys. Rev. Lett.* **98**, 065002 (2007).
- [25] Ray F Egerton, “Electron energy-loss spectroscopy in the tem,” *Reports on Progress in Physics* **72**, 016502 (2008).
- [26] Ho kwang Mao, Chichang Kao, and Russell J Hemley, “Inelastic x-ray scattering at ultrahigh pressures,” *Journal of Physics: Condensed Matter* **13**, 7847–7858 (2001).
- [27] Katerina Falk, “Experimental methods for warm dense matter research,” *High Power Laser Science and Engineering* **6**, e59 (2018).
- [28] Christoph Bostedt, Sébastien Boutet, David M. Fritz, Zhirong Huang, Hae Ja Lee, Henrik T. Lemke, Aymeric Robert, William F. Schlotter, Joshua J. Turner, and Garth J. Williams, “Linac coherent light source: The first five years,” *Rev. Mod. Phys.* **88**, 015007 (2016).
- [29] Thomas Tschentscher, Christian Bressler, Jan Grünert, Anders Madsen, Adrian P. Mancuso, Michael Meyer, Andreas Scherz, Harald Sinn, and Ulf Zastra, “Photon beam transport and scientific instruments at the european xfel,” *Applied Sciences* **7** (2017).
- [30] E. I. Moses, R. N. Boyd, B. A. Remington, C. J. Keane, and R. Al-Ayat, “The national ignition facility: ushering in a new age for high energy density science,” *Physics of Plasmas* **16**, 041006 (2009), <https://doi.org/10.1063/1.3116505>.
- [31] D. Kraus, J. Vorberger, A. Pak, N. J. Hartley, L. B. Fletcher, S. Frydrych, E. Galtier, E. J. Gamboa, D. O. Gericke, S. H. Glenzer, E. Granados, M. J. MacDonald, A. J. MacKinnon, E. E. McBride, I. Nam, P. Neumayer, M. Roth, A. M. Saunders, A. K. Schuster, P. Sun, T. van Driel, T. Döppner, and R. W. Falcone, “Formation of diamonds in laser-compressed hydrocarbons at planetary interior conditions,” *Nature Astronomy* **1**, 606–611 (2017).

- [32] M. D. Knudson, M. P. Desjarlais, A. Becker, R. W. Lemke, K. R. Cochrane, M. E. Savage, D. E. Bliss, T. R. Mattsson, and R. Redmer, “Direct observation of an abrupt insulator-to-metal transition in dense liquid deuterium,” *Science* **348**, 1455–1460 (2015).
- [33] R. Ernstorfer, M. Harb, C. T. Hebeisen, G. Sciaini, T. Dartigalongue, and R. J. D. Miller, “The formation of warm dense matter: Experimental evidence for electronic bond hardening in gold,” *Science* **323**, 1033 (2009).
- [34] L. B. Fletcher, A. L. Kritcher, A. Pak, T. Ma, T. Döppner, C. Fortmann, L. Divol, O. S. Jones, O. L. Landen, H. A. Scott, J. Vorberger, D. A. Chapman, D. O. Gericke, B. A. Mattern, G. T. Seidler, G. Gregori, R. W. Falcone, and S. H. Glenzer, “Observations of continuum depression in warm dense matter with x-ray thomson scattering,” *Phys. Rev. Lett.* **112**, 145004 (2014).
- [35] S. Frydrych, J. Vorberger, N. J. Hartley, A. K. Schuster, K. Ramakrishna, A. M. Saunders, T. van Driel, R. W. Falcone, L. B. Fletcher, E. Galtier, E. J. Gamboa, S. H. Glenzer, E. Granados, M. J. MacDonald, A. J. MacKinnon, E. E. McBride, I. Nam, P. Neumayer, A. Pak, K. Voigt, M. Roth, P. Sun, D. O. Gericke, T. Döppner, and D. Kraus, “Demonstration of x-ray thomson scattering as diagnostics for miscibility in warm dense matter,” *Nature Communications* **11**, 2620 (2020).
- [36] Siegfried H. Glenzer and Ronald Redmer, “X-ray thomson scattering in high energy density plasmas,” *Rev. Mod. Phys.* **81**, 1625–1663 (2009).
- [37] Dietrich Kremp, Manfred Schlanges, and Wolf-Dietrich Kraeft, *Quantum Statistics of Nonideal Plasmas*, Springer Series on Atomic, Optical, and Plasma Physics (Springer, Berlin, Heidelberg, 2005).
- [38] R. Thiele, T. Bornath, C. Fortmann, A. Höll, R. Redmer, H. Reinholz, G. Röpke, A. Wierling, S. H. Glenzer, and G. Gregori, “Plasmon resonance in warm dense matter,” *Physical Review E* **78**, 026411 (2008).
- [39] N. David Mermin, “Lindhard dielectric function in the relaxation-time approximation,” *Physical Review B* **1**, 2362 (1970).
- [40] H. Reinholz, R. Redmer, G. Röpke, and A. Wierling, “Long-wavelength limit of the dynamical local-field factor and dynamical conductivity of a two-component plasma,” *Phys. Rev. E* **62**, 5648–5666 (2000).
- [41] Carsten Fortmann, August Wierling, and Gerd Röpke, “Influence of local-field corrections on thomson scattering in collision-dominated two-component plasmas,” *Phys. Rev. E* **81**, 026405 (2010).
- [42] Ryogo Kubo, “Statistical-mechanical theory of irreversible processes. i. general theory and simple applications to magnetic and conduction problems,” *Journal of the Physical Society of Japan* **12**, 570–586 (1957).
- [43] D. A. Greenwood, “The boltzmann equation in the theory of electrical conduction in metals,” *Proceedings of the Physical Society* **71**, 585 (1958).
- [44] B. B. L. Witte, L. B. Fletcher, E. Galtier, E. Gamboa, H. J. Lee, U. Zastra, R. Redmer, S. H. Glenzer, and P. Sperling, “Warm dense matter demonstrating non-drude conductivity from observations of nonlinear plasmon damping,” *Phys. Rev. Lett.* **118**, 225001 (2017).
- [45] Kushal Ramakrishna and Jan Vorberger, “Ab initio dielectric response function of diamond and other relevant high pressure phases of carbon,” *Journal of Physics: Condensed Matter* **32**, 095401 (2019).
- [46] M.A.L. Marques and E.K.U. Gross, “Time-dependent density functional theory,” *Annual Review of Physical Chemistry* **55**, 427–455 (2004), pMID: 15117259.
- [47] Marco Cazzaniga, Hans-Christian Weissker, Simo Huotari, Tuomas Pylkkänen, Paolo Salvestrini, Giulio Monaco, Giovanni Onida, and Lucia Reining, “Dynamical response function in sodium and aluminum from time-dependent density-functional theory,” *Phys. Rev. B* **84**, 075109 (2011).
- [48] Kushal Ramakrishna, Tobias Dornheim, and Jan Vorberger, “Influence of finite temperature exchange-correlation effects in hydrogen,” *Phys. Rev. B* **101**, 195129 (2020).
- [49] A. D. Baczewski, L. Shulenburger, M. P. Desjarlais, S. B. Hansen, and R. J. Magyar, “X-ray thomson scattering in warm dense matter without the chihara decomposition,” *Phys. Rev. Lett.* **116**, 115004 (2016).
- [50] Tobias Dornheim, Jan Vorberger, Simon Groth, Nico Hoffmann, Zh. A. Moldabekov, and Michael Bonitz, “The static local field correction of the warm dense electron gas: An ab initio path integral monte carlo study and machine learning representation,” *The Journal of chemical physics* **151**, 194104 (2019).
- [51] Ali Abedi, Neepa T. Maitra, and E. K. U. Gross, “Correlated electron-nuclear dynamics: Exact factorization of the molecular wavefunction,” *The Journal of Chemical Physics* **137**, 22A530 (2012), <https://doi.org/10.1063/1.4745836>.
- [52] Jenő Sólyom, *Fundamentals of the Physics of Solids* (Springer Berlin Heidelberg, 2010).
- [53] Paul Hamann, Tobias Dornheim, Jan Vorberger, Zhandos A. Moldabekov, and Michael Bonitz, “Dynamic properties of the warm dense electron gas: an ab initio path integral monte carlo approach,” (2020), [arXiv:2007.15471 \[physics.comp-ph\]](https://arxiv.org/abs/2007.15471).
- [54] Chongjie Mo, Zhenguo Fu, Wei Kang, Ping Zhang, and X. T. He, “First-principles estimation of electronic temperature from x-ray thomson scattering spectrum of isochorically heated warm dense matter,” *Phys. Rev. Lett.* **120**, 205002 (2018).
- [55] Michael Bonitz, *Quantum Kinetic Theory, 2nd edition* (Springer, Berlin, Heidelberg, 2016).
- [56] Paul Hamann, Jan Vorberger, Tobias Dornheim, Zhandos Moldabekov, and Michael Bonitz, “Ab initio results for the plasmon dispersion and damping of the warm dense electron gas,” (2020), [arXiv:2008.04605 \[physics.plasm-ph\]](https://arxiv.org/abs/2008.04605).
- [57] David Pines and David Bohm, “A collective description of electron interactions: Ii. collective vs individual particle aspects of the interactions,” *Physical Review* **85**, 338 (1952).
- [58] David Bohm and David Pines, “A collective description of electron interactions: Iii. coulomb interactions in a degenerate electron gas,” *Physical Review* **92**, 609 (1953).
- [59] W.D. Kraeft, W. Ebeling, D. Kremp, and G. Röpke, *Quantum Statistics of Charged Particle Systems* (Springer, 1986).
- [60] Leo P. Kadanoff and Gordon Baym, *Quantum Statistical Mechanics* (Perseus, 1962).
- [61] David Pines, *Elementary excitations in solids* (CRC Press, 2018).
- [62] K. J. Krane, “Dispersion and damping of volume plasmons in polycrystalline aluminium and indium,” *Journal of Physics F: Metal Physics* **8**, 2133–2137 (1978).

- [63] T. Dornheim, S. Groth, J. Vorberger, and M. Bonitz, “Ab initio path integral monte carlo results for the dynamic structure factor of correlated electrons: From the electron liquid to warm dense matter,” *Phys. Rev. Lett.* **121**, 255001 (2018).
- [64] S. Groth, T. Dornheim, and J. Vorberger, “Ab initio path integral monte carlo approach to the static and dynamic density response of the uniform electron gas,” *Phys. Rev. B* **99**, 235122 (2019).
- [65] Tobias Dornheim and Jan Vorberger, “Finite-size effects in the reconstruction of dynamic properties from ab initio path integral monte-carlo simulations,” (2020), [arXiv:2004.13429 \[cond-mat.str-el\]](https://arxiv.org/abs/2004.13429).
- [66] T. Dornheim, J. Vorberger, S. Groth, N. Hoffmann, Zh. A. Moldabekov, and M. Bonitz, “The static local field correction of the warm dense electron gas: An ab initio path integral monte carlo study and machine learning representation,” *The Journal of Chemical Physics* **151**, 194104 (2019).
- [67] Saverio Moroni, David M. Ceperley, and Gaetano Senatore, “Static response from quantum monte carlo calculations,” *Phys. Rev. Lett.* **69**, 1837–1840 (1992).
- [68] Saverio Moroni, David M. Ceperley, and Gaetano Senatore, “Static response and local field factor of the electron gas,” *Phys. Rev. Lett.* **75**, 689–692 (1995).
- [69] Massimiliano Corradini, Rodolfo Del Sole, Giovanni Onida, and Maurizia Palumbo, “Analytical expressions for the local-field factor  $g(q)$  and the exchange-correlation kernel  $K_{xc}(r)$  of the homogeneous electron gas,” *Phys. Rev. B* **57**, 14569–14571 (1998).
- [70] Valentin V. Karasiev, Lázaro Calderín, and S. B. Trickey, “Importance of finite-temperature exchange correlation for warm dense matter calculations,” *Phys. Rev. E* **93**, 063207 (2016).
- [71] Tobias Dornheim, Attila Cangi, Kushal Ramakrishna, Maximilian Böhme, Shigenori Tanaka, and Jan Vorberger, “Effective static approximation: A fast and reliable tool for warm dense matter theory,” (2020), [arXiv:2008.02165 \[physics.plasm-ph\]](https://arxiv.org/abs/2008.02165).
- [72] Tobias Dornheim, Travis Sjoström, Shigenori Tanaka, and Jan Vorberger, “Strongly coupled electron liquid: Ab initio path integral monte carlo simulations and dielectric theories,” *Phys. Rev. B* **101**, 045129 (2020).
- [73] Tobias Dornheim, Zhandos A. Moldabekov, Jan Vorberger, and Simon Groth, “Ab initio path integral monte carlo simulation of the uniform electron gas in the high energy density regime,” *Plasma Physics and Controlled Fusion* **62**, 075003 (2020).
- [74] W. Kohn and L. J. Sham, “Self-consistent equations including exchange and correlation effects,” *Phys. Rev.* **140**, A1133–A1138 (1965).
- [75] Aurora Pribram-Jones, David A. Gross, and Kieron Burke, “Dft: A theory full of holes?” *Annual Review of Physical Chemistry* **66** (2015), 10.1146/annurev-physchem-040214-121420.
- [76] N. David Mermin, “Thermal properties of the inhomogeneous electron gas,” *Phys. Rev.* **137**, A1441–A1443 (1965).
- [77] E. K. U. Gross and Walter Kohn, “Local density-functional theory of frequency-dependent linear response,” *Phys. Rev. Lett.* **55**, 2850–2852 (1985).
- [78] G. Kresse and J. Hafner, “Ab initio molecular dynamics for liquid metals,” *Phys. Rev. B* **47**, 558–561 (1993).
- [79] G. Kresse and D. Joubert, “From ultrasoft pseudopotentials to the projector augmented-wave method,” *Phys. Rev. B* **59**, 1758–1775 (1999).
- [80] G. Kresse and J. Furthmüller, “Efficiency of ab-initio total energy calculations for metals and semiconductors using a plane-wave basis set,” *Computational Materials Science* **6**, 15 – 50 (1996).
- [81] G. Kresse and J. Furthmüller, “Efficient iterative schemes for ab initio total-energy calculations using a plane-wave basis set,” *Phys. Rev. B* **54**, 11169–11186 (1996).
- [82] W. Schülke, H. Schulte-Schrepping, and J. R. Schmitz, “Dynamic structure of electrons in Al metal studied by inelastic x-ray scattering,” *Phys. Rev. B* **47**, 12426–12436 (1993).
- [83] J. Z. Tischler, B. C. Larson, P. Zschack, A. Fleszar, and A. G. Eguluz, “Interplay between inelastic x-ray scattering and ab initio density-response calculations: Insight into the electronic correlations in aluminum,” *physica status solidi (b)* **237**, 280–288 (2003).
- [84] B. C. Larson, J. Z. Tischler, E. D. Isaacs, P. Zschack, A. Fleszar, and A. G. Eguluz, “Inelastic x-ray scattering as a probe of the many-body local-field factor in metals,” *Phys. Rev. Lett.* **77**, 1346–1349 (1996).
- [85] Andrzej Fleszar, Andrew A Quong, and Adolfo G Eguluz, “Band-structure and many-body effects in the dynamical response of aluminum metal,” *Physical review letters* **74**, 590 (1995).
- [86] Martin Panholzer, Matteo Gatti, and Lucia Reining, “Nonlocal and nonadiabatic effects in the charge-density response of solids: A time-dependent density-functional approach,” *Phys. Rev. Lett.* **120**, 166402 (2018).
- [87] C. Sternemann, S. Huotari, G. Vankó, M. Volmer, G. Monaco, A. Gusarov, H. Lustfeld, K. Sturm, and W. Schülke, “Correlation-induced double-plasmon excitation in simple metals studied by inelastic x-ray scattering,” *Phys. Rev. Lett.* **95**, 157401 (2005).
- [88] S Huotari, C Sternemann, W Schülke, K Sturm, H Lustfeld, H Sternemann, M Volmer, A Gusarov, H Müller, and G Monaco, “Electron-density dependence of double-plasmon excitations in simple metals,” *Physical Review B* **77**, 195125 (2008).
- [89] E Petri, A Otto, and W Hanke, “Anisotropy of plasmon dispersion in Al: An electron correlation effect,” *Solid State Communications* **19**, 711–714 (1976).
- [90] K. Sturm and A. Gusarov, “Dynamical correlations in the electron gas,” *Phys. Rev. B* **62**, 16474–16491 (2000).
- [91] KC Pandey, PM Platzman, P Eisenberger, and E-Ni Foo, “Plasmons in periodic solids,” *Physical Review B* **9**, 5046 (1974).
- [92] J. Sprösser-Prou, A. vom Felde, and J. Fink, “Aluminum bulk-plasmon dispersion and its anisotropy,” *Phys. Rev. B* **40**, 5799–5801 (1989).
- [93] P. E. Batson and J. Silcox, “Experimental energy-loss function,  $\text{Im}[-\frac{1}{\epsilon}(q, \omega)]$ , for aluminum,” *Phys. Rev. B* **27**, 5224–5239 (1983).
- [94] HJ Höhberger, A Otto, and E Petri, “Plasmon resonance in Al, deviations from quadratic dispersion observed,” *Solid State Communications* **16**, 175–179 (1975).
- [95] J. A. Budagosky and E. E. Krasovskii, “All-electron product basis set: Application to plasmon anisotropy in simple metals,” *Phys. Rev. B* **99**, 245149 (2019).

- [96] Keun-Ho Lee and K. J. Chang, “First-principles study of the optical properties and the dielectric response of al,” *Phys. Rev. B* **49**, 2362–2367 (1994).
- [97] Andrew A. Quong and Adolfo G. Eguiluz, “First-principles evaluation of dynamical response and plasmon dispersion in metals,” *Phys. Rev. Lett.* **70**, 3955–3958 (1993).
- [98] David Pines, *Theory of Quantum Liquids: Normal Fermi Liquids* (CRC Press, 2018).
- [99] Setsuo Ichimaru, “Strongly coupled plasmas: high-density classical plasmas and degenerate electron liquids,” *Reviews of Modern Physics* **54**, 1017 (1982).
- [100] Lev Davidovich Landau, “On the vibrations of the electronic plasma,” *Zh. Eksp. Teor. Fiz.* **10**, 25 (1946).
- [101] Miguel Marques, Carsten A Ullrich, Fernando Nogueira, Angel Rubio, Kieron Burke, and Eberhard KU Gross, *Time-dependent density functional theory* (Springer Berlin, 2006).
- [102] C. v. Festenberg, “Zur dämpfung des al-15 ev-plasmaverlustes in abhängigkeit vom streuwinkel und der kristallitgröße,” *Zeitschrift für Physik* **207**, 47–55 (1967).
- [103] T. Kloos, “Plasmaschwingungen in al, mg, li, na und k angeregt durch schnelle elektronen,” *Zeitschrift für Physik A Hadrons and nuclei* **265**, 225–238 (1973).
- [104] PC Gibbons, SE Schnatterly, JJ Ritsko, and JR Fields, “Line shape of the plasma resonance in simple metals,” *Physical Review B* **13**, 2451 (1976).
- [105] RK Pal and DN Tripathy, “Plasmon dispersion and linewidth in aluminium,” *Pramana* **24**, 905–910 (1985).
- [106] Peter Jewsbury, “Theoretical analysis of plasmon dispersion in simple metals,” *Australian Journal of Physics* **32**, 361–368 (1979).
- [107] P. Sperling, E. J. Gamboa, H. J. Lee, H. K. Chung, E. Galtier, Y. Omarbakiyeva, H. Reinholz, G. Röke, U. Zastrau, J. Hastings, L. B. Fletcher, and S. H. Glenzer, “Free-electron x-ray laser measurements of collisional-damped plasmons in isochorically heated warm dense matter,” *Phys. Rev. Lett.* **115**, 115001 (2015).
- [108] T. R. Preston, K. Appel, E. Brambrink, B. Chen, L. B. Fletcher, C. Fortmann-Grote, S. H. Glenzer, E. Granados, S. Göde, Z. Konôpková, H. J. Lee, H. Marquardt, E. E. McBride, B. Nagler, M. Nakatsutsumi, P. Sperling, B. B. L. Witte, and U. Zastrau, “Measurements of the momentum-dependence of plasmonic excitations in matter around 1 mbar using an x-ray free electron laser,” *Applied Physics Letters* **114**, 014101 (2019).
- [109] B. B. L. Witte, P. Sperling, M. French, V. Recoules, S. H. Glenzer, and R. Redmer, “Observations of non-linear plasmon damping in dense plasmas,” *Physics of Plasmas* **25**, 056901 (2018), <https://doi.org/10.1063/1.5017889>.
- [110] J. K. Dewhurst et al., “Elk, all-electron full-potential linearised augmented plane wave (fp-lapw) code,” <http://elk.sourceforge.net/> (2020).
- [111] Peter E Blöchl, “Projector augmented-wave method,” *Physical review B* **50**, 17953 (1994).
- [112] John P Perdew, Kieron Burke, and Matthias Ernzerhof, “Generalized gradient approximation made simple,” *Physical review letters* **77**, 3865 (1996).
- [113] William G. Hoover, “Canonical dynamics: Equilibrium phase-space distributions,” *Phys. Rev. A* **31**, 1695–1697 (1985).
- [114] Paolo Giannozzi, Stefano Baroni, Nicola Bonini, Matteo Calandra, Roberto Car, Carlo Cavazzoni, Davide Ceresoli, Guido L Chiarotti, Matteo Cococcioni, Ismaila Dabo, et al., “Quantum espresso: a modular and open-source software project for quantum simulations of materials,” *Journal of physics: Condensed matter* **21**, 395502 (2009).
- [115] Paolo Giannozzi, Oliviero Andreussi, Thomas Brumme, Oana Bunau, M Buongiorno Nardelli, Matteo Calandra, Roberto Car, Carlo Cavazzoni, Davide Ceresoli, Matteo Cococcioni, et al., “Advanced capabilities for materials modelling with quantum espresso,” *Journal of Physics: Condensed Matter* **29**, 465901 (2017).
- [116] “Opium - pseudopotential generation project,” <http://opium.sourceforge.net/>.
- [117] M. Methfessel and A. T. Paxton, “High-precision sampling for brillouin-zone integration in metals,” *Phys. Rev. B* **40**, 3616–3621 (1989).
- [118] Andrea Marini, Conor Hogan, Myrta Grüning, and Daniele Varsano, “yambo: An ab initio tool for excited state calculations,” *Computer Physics Communications* **180**, 1392 – 1403 (2009).
- [119] Dario Rocca, Ralph Gebauer, Yousef Saad, and Stefano Baroni, “Turbo charging time-dependent density-functional theory with lanczos chains,” *The Journal of Chemical Physics* **128**, 154105 (2008).
- [120] Iurii Timrov, Nathalie Vast, Ralph Gebauer, and Stefano Baroni, “Electron energy loss and inelastic x-ray scattering cross sections from time-dependent density-functional perturbation theory,” *Phys. Rev. B* **88**, 064301 (2013).
- [121] Iurii Timrov, Nathalie Vast, Ralph Gebauer, and Stefano Baroni, “turboeels—a code for the simulation of the electron energy loss and inelastic x-ray scattering spectra using the liouville–lanczos approach to time-dependent density-functional perturbation theory,” *Computer Physics Communications* **196**, 460 – 469 (2015).